

---

# REINFORCEMENT LEARNING-BASED ADAPTIVE TIME-INTEGRATION FOR NONSMOOTH DYNAMICS

---

**David Michael Riley\***

IMSIA, CEA, CNRS, EDF, ENSTA Paris, Institut Polytechnique de Paris,  
91120 Palaiseau, France  
david.riley@ensta.fr

**Alexandros Stathas**

Institute of Structural Engineering, BOKU, Peter-Jordan-Straße 82,  
1190 Wien, Austria  
alexandros.stathas@boku.ac.at

**Diego Gutiérrez-Oribio**

IMSIA, CEA, CNRS, EDF, ENSTA Paris, Institut Polytechnique de Paris,  
91120 Palaiseau, France  
diego.gutierrez@ensta.fr

**Ioannis Stefanou**

IMSIA, CEA, CNRS, EDF, ENSTA Paris, Institut Polytechnique de Paris,  
91120 Palaiseau, France  
ioannis.stefanou@ensta.fr

January 16, 2025

## ABSTRACT

Numerical time integration is fundamental to the simulation of initial and boundary value problems. Traditionally, time integration schemes require adaptive time-stepping to ensure computational speed and sufficient accuracy. Although these methods are based on mathematical derivations related to the order of accuracy for the chosen integrator, they also rely on heuristic development to determine optimal time steps. In this work, we use an alternative approach based on Reinforcement Learning (RL) to select the optimal time step for any time integrator method, balancing computational speed and accuracy. To explore the potential of our RL-based adaptive time-stepping approach, we choose a challenging model problem involving set-valued frictional instabilities at various spatiotemporal scales. This problem demonstrates the robustness of our strategy in handling nonsmooth problems, which present a demanding scenario for numerical integration. Specifically, we apply RL to the simulation of a seismic fault with Coulomb friction. Our findings indicate that RL can learn an optimal strategy for time integration, achieving up to a fourfold speed-up. Our RL-based adaptive integrator offers a new approach for time integration in various other problems in mechanics.

**Keywords** Reinforcement learning · numerical integration · adaptive time stepping · nonsmooth dynamics

---

\*Corresponding author: david.riley@ensta.fr

# 1 Introduction

Many problems in physical systems have evolution equations that can be nonsmooth and are not analytically solvable, consequently requiring numerical integration. Such nonsmooth phenomena exhibit abrupt state changes that challenge numerical integration methods, and they arise in many fields, including mechanics [1, 2], electrical circuits [2, 3], biology [3], and several areas [4]. Furthermore, sliding-mode controllers, designed to reject diverse perturbations using set-valued functions [5], introduce additional nonsmooth behavior in closed-loop systems, even when the original dynamics are smooth. This interplay of inherent system nonsmoothness and controller-induced discontinuities underscores the need for robust and efficient time integration algorithms.

Conventional time integration techniques, which resolve the time evolution of dynamical systems [6], typically rely on constant time stepping. However, the accuracy and efficiency of such methods are highly dependent on the chosen time step. While constant time stepping is straightforward, it can prove computationally intensive, especially for stiff systems or systems with several spatiotemporal scales that are common in nonsmooth dynamics.

To address the computational inefficiency of constant time-stepping, adaptive integration methods have been developed [7, 6]. There are generally two frameworks under which adaptive time integration can be undertaken. The first is self-adaptive methods, such as adaptive Runge-Kutta schemes, which utilize internal information to adjust the time-step [6, 8]. An alternative approach involves estimating local errors by comparing the solutions from one large time step with those from two smaller time steps, known as Richardson extrapolation [6]. While these methods have mathematical foundations, they rely on local approximations of the error, implying that they are neither exact nor perfect. To enhance these methods, research has introduced heuristic parameters to ensure that the time-step neither changes too slowly nor rapidly, which often requires careful empirical tuning [9]. Moreover, smoothness is critical to the assumptions of conventional adaptive integrators. For stiff and nonsmooth systems, additional considerations must be considered, such as order reduction of the integrator [2, 10] or loss of differentiability [11]. To combat these phenomena for constrained mechanical systems, adaptive integrators have been proposed that attempt to predict the switching of constraints [2, 11]. However, in large systems, tracking constraint switching leads to additional computational overhead, and conflicting results of computational speed improvements yield the benefits of this method unclear [2].

Yet another alternative is based on the mathematical theory of control [12]. These methodologies rely on designing a controller to choose the appropriate step size to achieve a given accuracy [13, 10]. Control-theoretic methods have generally focused on ensuring a smooth time-step evolution rather than computational speed. Moreover, they require distinct control laws tailored for stiff and nonstiff ODEs [10]. Thus, control-based time steppers are not well suited for the use of general mechanical systems.

Recently, with the advancement of machine learning, research has focused on replacing conventional methods with data-driven approaches. For example, neural ordinary differential equations (neural ODEs) have been proposed to learn a mapping from a current time to a unit forward in time, enhancing accuracy and computational efficiency [14]. An alternative approach involves using reinforcement learning (RL) to learn the adaptive time-stepping policy. The combination of deep learning with multiscale time stepping has shown significant improvement over traditional methods when using full state observation of the ODE [15], suggesting that deep learning could be used to accelerate the efficiency of time-steppers in general. More recently, deep learning was applied to select the optimal time step from a discrete predefined set for chaotic, smoothly varying ODEs using explicit integration [16]. Similarly, a RL-based explicit adaptive time stepper with a continuous action space was developed for a multiphysics particle simulation to improve computational speed while maintaining comparable accuracy [17, 18]. Alternative studies have investigated the application of a RL-based implicit adaptive time-stepping method, where two independent neural networks were used: one responsible for stepping forward in time and another for stepping back in time if the nonlinear solver did not converge in simulations of electrical circuits [19, 20]. While this dual-network structure performs well for smooth problems, the use of a forward/backward stepping strategy could be avoided, given the potential of current methods in machine learning. More broadly, although the aforementioned approaches represent fundamental achievements in the time integration of smooth numerical problems, they do not exploit the significant potential of reinforcement learning for non-smooth mechanical systems, which is the focus of the current work.

More specifically, this paper develops an RL-based approach for adaptive time-stepping of nonsmooth mechanical systems using a single Truncated Quantile Critics (TQC) network, leveraging the robustness of TQC for continuous action spaces [21]. This single-network approach not only simplifies the architecture compared to the dual-network strategy but also provides a general implementation suitable for both explicit and implicit integration schemes. The extension of RL-based adaptive time-stepping approaches to nonsmooth mechanics problems enables the methodology, for the first time, to efficiently integrate dynamical systems with discontinuities and set-valued right-hand sides. As an example, we focus on dynamical systems with Coulomb friction systems which are inherently challenging given their unstable, stick and slip behavior. Our findings suggest that the RL-based approach, combined with variational

inequalities for solving the nonsmooth mechanical systems [2], establishes a general framework for learning efficient and accurate policies for adaptive time-stepping that can be applied across a diverse range of complex mechanical systems.

This paper is organized as follows. In Section 2, the general form of the type of mechanical dynamical systems that are relevant to this paper are introduced. Section 3 provides a brief introduction to the heuristic-based policy. Following suit, Section 4 introduces the reinforcement learning algorithm employed, and, finally, the performance of the RL-based method is showcased with an example scenario in Section 5.

## 2 Problem description

To explore the potential of reinforcement learning for adaptive time-stepping policies, we investigate mechanical systems characterized by the linear momentum equation:

$$M\dot{v} = -F_r + F_{int}, \quad (1)$$

where  $v \in \mathbb{R}^N$  is the velocity vector,  $\dot{\square} = \frac{\partial}{\partial t}$  is the time derivative,  $F_r \in \mathbb{R}^N$  represents general constraint forces,  $M_{++}^N$  is the mass matrix,  $F_{int} \in \mathbb{R}^N$  is the vector of internal forces, and  $N$  is the number of degrees of freedom. This formulation applies to a wide range of constrained holonomic and/or non-holonomic mechanical systems.

There are a few approaches to performing numerical simulations that satisfy these mechanical constraints. The classical approaches involve enforcing the constraints through penalty formulations or via Lagrangian constraints [22, 23, 24]. Alternatively, leveraging concepts from convex analysis, constraints can be reformulated into variational inequalities, which allows for their accurate and efficient enforcement [2, 25].

In this paper, we adopt the latter method, wherein the constraints and their normal inclusion equivalents are detailed in Section 5. Finally, the integration scheme used within this paper is the Bathe method [26, 27], which provides numerical damping of high-frequency content while maintaining both low-frequency content and second-order accuracy. However, the methodology applied within this paper can be applied to alternative time-stepping methods as well.

## 3 Heuristic-based adaptive time-stepping

To evaluate the effectiveness of our reinforcement learning-based adaptive time-stepping policy, we first introduce the heuristic-based adaptive time-stepping method commonly used in the numerical integration of ODEs. This method will serve as a baseline for comparison.

Adaptive time-stepping methods dynamically adjust the time step to balance computational efficiency and accuracy. They estimate local errors by comparing the solutions obtained from one large time step with those from two smaller steps, as discussed in [6]. This approach is beneficial for maintaining accuracy while avoiding unnecessary computational effort in systems where the dynamics change rapidly.

By first performing a Taylor series expansion of the integration scheme, the local error  $e_k$  can be approximated by:

$$e_k = \frac{x_{1/2} - x_1}{2^p - 1}, \quad (2)$$

where  $x_1$  is the solution after one large time-step,  $x_{1/2}$  is the solution after two smaller steps, which are half of the large time-step, and  $p$  is the order of the integration method. The relative error measure can then be expressed as [6, 2]

$$E_r = |e_k \cdot \text{tol}^{-1}|, \quad (3)$$

where  $\text{tol}$  is a specified tolerance for error control. Thus, the optimal time-step is given by [6, 8, 2]:

$$h_{opt} = h \left( \frac{1}{E_r} \right)^q, \quad (4)$$

where  $q = \frac{1}{2^p - 1}$  and  $h$  is the previous time-step size.

To ensure stability and accuracy, the optimal time-step is adjusted using a heuristic rule that prevents the time-step increment from experiencing extreme variations. The empirical based update for the time-step,  $\Delta t_{\text{next}}$ , is given by [6, 9]:

$$\Delta t_{\text{next}} = \begin{cases} \min(h \cdot E_r^{-q}, h_{\max}), & \text{if success and } E_r > 1, \\ \max(h \cdot \min(c_{\text{up}}, E_r^{-q}), h_{\min}, t_{\max} - t), & \text{if success and } E_r \leq 1, \\ h \cdot c_{\text{down}}, & \text{if not success and } h > h_{\min}, \\ \text{Abort}, & \text{otherwise.} \end{cases} \quad (5)$$

Here,  $h_{\min}$  and  $h_{\max}$  are bounds on  $h$ .  $c_{\text{up}}$  and  $c_{\text{down}}$  are scaling factors for increasing and decreasing the time-step size, which are determined empirically.

While this methodology is effective for smooth integration problems, the processes studied in this paper are generally nonsmooth. Nonsmooth dynamics involve abrupt changes in the system’s behavior, making it challenging for traditional adaptive methods to maintain accuracy without high computational costs. Although conventional heuristic-based methods are not well-tuned for nonsmooth dynamics, we apply the conventional heuristic-based adaptive time-stepping method as a baseline for comparison with our reinforcement learning-based adaptive time-stepping policy. This comparison allows us to evaluate the advantages of the RL approach in handling nonsmooth dynamics.

## 4 Reinforcement learning

Reinforcement learning (RL) is a branch of machine learning where an agent learns to make decisions by interacting with an environment to maximize a cumulative reward [28, 29, 30]. In the context of adaptive time-stepping, the RL agent aims to learn a policy that selects optimal time steps to balance computational speed (or run time) and solution accuracy.

### 4.1 Architecture

We utilize the Truncated Quantile Critics (TQC) algorithm [21] implemented within Stable-Baselines3 [31], which excels in continuous control tasks, where actions are chosen from a continuous range rather than from a set of discrete options. Traditional RL algorithms predict just an average expected outcome (the “return”). Instead, the TQC estimates a full range of possible outcomes and how likely they are, providing a complete probability distribution of these returns. By truncating overly optimistic estimates, TQC creates a more stable and accurate assessment of future performance compared to more conventional methods such as the Twin Delayed Deep Deterministic Policy Gradient (TD3) algorithm [32]. Note an overview of the general training procedure of the TQC network is provided in Section 4.4.

Here, we use an actor network with two hidden layers, each with 64 nodes, and a critic network with three hidden layers with 64 nodes. The larger number of hidden layers in the critic network is thought to enhance the agent’s ability to accurately evaluate actions in environments with nonsmooth dynamics. Furthermore, following the original paper [21], we employed five critic networks to provide a more robust estimation of the return distribution. Finally, we used generalized State-Dependent Exploration to ensure a balanced exploration of the action space exploiting learned patterns. All hyperparameters other than those discussed above take default values according to StableBaselines3 [31]. A summary of the hyperparameters used for the TQC algorithm is listed in Table 1.

Table 1: TQC hyperparameters used in the reinforcement learning environment.

Hyperparameter	Value
Actor network size	(64,64)
Critic network size	(64,64,64)
Number of critic networks	5
Learning rate	$3 \times 10^{-4}$
Buffer size	$10^6$
Batch size	256
Discount factor ( $\gamma$ )	0.99
Polyak coefficient ( $\tau$ )	0.005
Generalized state-dependent exploration	True

### 4.2 Reward function

The reward function aims to reward both a fast run time and solution accuracy by taking the product of the computational time of a single time step and relative error (see Eq. (3)) in a multiplicative manner. The first term rewards large time steps, which encourages fast simulations by accounting for the step size chosen relative to the maximum and minimum time step sizes. However, this may result in a large number of nonlinear iterations, thus compromising the overall speed of a given step. To mitigate this factor, the second term rewards faster runtimes of an individual time step by taking its runtime relative to the maximum possible runtime and minimum possible runtime. To reward an accurate time step, these terms are multiplied by a negative exponential of the relative error  $E_r$ . Finally, when a time step does not converge, a negative reward proportional to the attempted time step relative to the maximum and minimum time

step sizes is applied. This is done so that the RL-based policy learns to reduce the time step whenever a time step does not converge.

Thus, the reward function,  $R$ , is defined as:

$$R = \begin{cases} \left( \frac{h - h_{\min}}{h_{\max} - h_{\min}} \right) \left( \frac{t_{\max}^{rt} - t^{rt}}{t_{\max}^{rt} - t_{\min}^{rt}} \right) e^{-\alpha E_r}, & \text{if success,} \\ - \left( \frac{h - h_{\min}}{h_{\max} - h_{\min}} \right), & \text{otherwise.} \end{cases} \quad (6)$$

where  $h$  is the selected time-step,  $t^{rt}$  is the runtime of the current time-step,  $t_{\min}^{rt}$  and  $t_{\max}^{rt}$  are in principle the minimum and maximum runtime for a given simulation, respectively, and  $\alpha$  is a speed/accuracy trade-off parameter, whose role is explained below. Generally,  $t_{\min}^{rt}$  and  $t_{\max}^{rt}$  are unknown *a priori*. However,  $t_{\min}^{rt}$  can be easily determined by evaluating a time step that converges within a single iteration. The maximum runtime can be approximated based on the computational complexity of the solver. This rough estimation has been found to produce a trained network capable of learning an efficient policy that balances computational speed and accuracy.

The speed-accuracy trade-off parameter  $\alpha$  is the only free parameter in the reward function. This parameter effectively penalizes the reward function if the relative error  $E_r$  is large. For larger  $\alpha$ , the reward is expected to be highly sensitive to large  $E_r$  and, thus, encourages a more accurate solution.

Notably, the reward function has aspects similar to those of previous RL-based adaptive time-steppers. More specifically, the reward is structured such that it encourages the largest possible time-step [16], considers computational time [19, 20], and penalizes the reward given a measure of error [16]. However, the particular form is different than previous works, and notably, we apply negative rewards for scenarios in which the nonlinear iterations did not converge.

### 4.3 Observational space

A key advantage of the RL-based adaptive policy is its ability to learn intricate nonlinear relationships between the observations of the environment and action taken, which the conventional heuristic time-stepping methods have not been developed to do. To benefit from this, the observation space of the proposed RL approach is expanded to include physical quantities as well as quantities related to the nonlinear solver.

Previous works have enhanced the observational space by providing the neural network with several measures of the numerical performance, such as the number of nonlinear iterations, error of the nonlinear iterations, and the relative error of time-steps [19, 20]. To provide a notation of state, the right-hand side of the considered ODE has been passed as an observation in the case of scalar equations [20, 16] or a latent space representation of the full state generated by an autoencoder [17] were passed as apart of the observational space.

We take a similar approach here by providing the same measures of numerical performance to the neural network and include the normalized time-step  $\hat{h}$ . However, as we are concerned with a general number of  $N$ -dimensional states, we opt to provide simply the spatial average of the velocity state  $\bar{v}$  and the spatial average of the internal energy  $\bar{U}$  as opposed to providing either the entire state vector or compounding the complexity of the problem by training an autoencoder to reduce the full-state to a latent variable representation. To this end, the observational space is defined as,

$$\begin{aligned} \mathcal{O} &= \left\{ \hat{U}, \hat{v}, \frac{E_{iter}}{4}, E_r, \hat{h}, I \right\}, \\ \hat{U} &= \frac{\bar{U}}{U_c} \in [0, 1 + \epsilon], \\ \hat{v} &= \frac{\bar{v}}{v_{max}} \in [0, 1 + \epsilon], \\ \hat{h} &= \frac{h - h_{min}}{h_{max} - h_{min}}, \end{aligned}$$

where  $\hat{U}$  is the normalized internal energy,  $U_c$  is defined as some critical energy which is discussed in Section 5.1,  $\hat{v}$  is the normalized average velocity,  $I$  is a boolean function for whether convergence was achieved, and  $\epsilon$  is some small number to be discussed below,  $E_{iter}$  is the summation of the error returned from the iterative nonlinear solver, which is not equivalent to  $E_r$ . Note that the normalization by 4 was determined by experimentation to ensure that it did not exceed a value of 1.

Typically, the exact maximum value of the average velocity is unknown prior to the simulation. Similarly, the so-called critical internal energy  $U_c$  may vary or not be clearly defined. However, these parameters can typically be estimated given a particular mechanical problem, hence providing a normalization that typically yields a maximum normalized

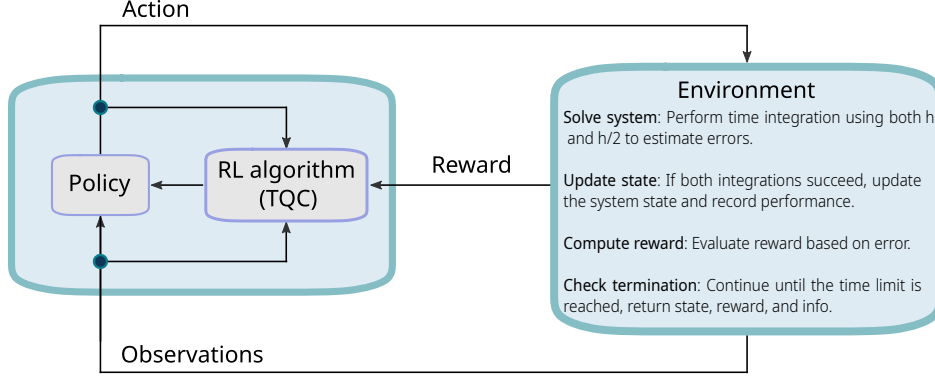


Figure 1: Illustration of the logic applied within the Reinforcement learning algorithm framework.

value of 1. Thus, we assume that the observational space may be a small value  $\epsilon$  beyond 1. More robust techniques could be devised such that the environment adaptively updates the normalization, but for the scenarios considered within this work, their use was unnecessary.

#### 4.4 General training procedure

The overall workflow of the algorithmic structure is illustrated in Figure 1, which shows the interplay between the policy (actor networks), the TQC algorithm, and the environment. For each attempted time step, the environment receives the current action, i.e., a proposed time step  $h$ , and advances with both a single large time step,  $t^{n+1} = t^n + h$ , and a substepping method with two smaller time steps of size  $\frac{h}{2}$ . These two integrations enable the environment to estimate the local error by Eq. (3), which is required for the reward. The environment updates the observational space, except for the states  $\hat{U}$  and  $\hat{v}$  if both integrators do not converge.

Following an attempted time step, the TQC algorithm generates a “transition“ comprised of the prior observations, the action taken, the resulting reward, and the updated observations, which is then stored in a replay buffer. Once a set number of transitions is collected, the TQC algorithm begins training at a specified interval. In our work, training occurs after each attempted time step, similar to previous studies of using RL-based adaptive time-integration [19, 20].

As mentioned above, the training procedure in the TQC algorithm as implemented by Stablebaselines3 [31] based on [21] is as follows. During training, the algorithm first calculates the target value by the sum of the immediate reward and the discounted estimate of the future returns. More specifically, copies of the critic networks, often called “target networks“, provide these estimates of future returns to avoid rapid swings in learning. Next, the difference between the predictions provided by the main critic networks and the target value are minimized via gradient descent, such that the critics updated parameters yield better predictions of the actual outcomes. To prevent abrupt shifts in the target estimates, the target networks parameters are slowly updated by a small factor termed the soft update coefficient (or Polyak coefficient),  $\tau = 0.005$ . The policy network’s parameters are then updated with gradient-based optimization to better choose time steps that yield higher returns to the main critics’ newly updated distributions, thereby maximizing the agent’s predicted long-term performance. For a more thorough discussion of the nuances within the algorithm, readers are referred to the original work [21].

Additionally, since the sensitivity of the speed-accuracy trade-off parameter  $\alpha$  (Eq. (6)) is not well understood, we perform a parametric analysis by training independent TQC networks for  $\alpha = \{2, 4, 8, 16\}$ . Finally, the number of training steps was manually explored and we found that 20,000 steps resulted in a plateau of the reward for all scenarios.

All TQC networks were trained on a laptop with the following specifications: processor AMD Ryzen 8945HS, 32 GB RAM, and an NVIDIA GeForce RTX 4070 Laptop GPU). Each training scenario took roughly seven minutes for the scenario in Section 5.1.1 and approximately two hours for the scenario in Section 5.5.

It should be stated here that the environment selects a time step based solely on the observational space, i.e., we do not enforce any changes to the time step that the network chooses as opposed to previous studies [20]. However, this lack of constraint on the policy implies that if the TQC network is not properly trained, then it may continually attempt time steps that may not converge, resulting in a constant observational space.

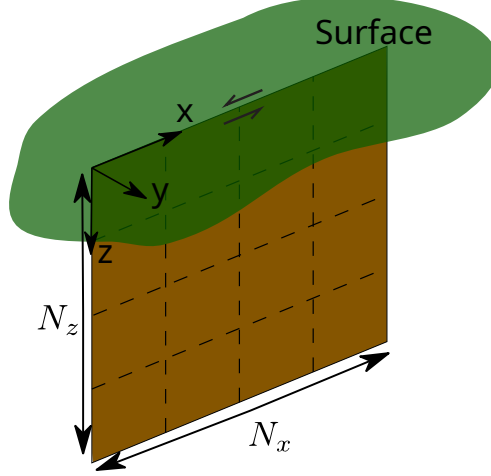


Figure 2: Sketch of a strike-slip fault configuration discretized in  $N_x \times N_z$  elements (modified from [33]).

## 5 RL performance

We evaluate the reinforcement learning algorithm’s general performance in handling nonsmooth dynamics. More specifically, to test the RL-based method’s robustness and adaptability, we simulate a challenging scenario in fault mechanics characterized by spatiotemporal Coulomb frictional instabilities. It is worth emphasizing that all simulations employ Bathe’s implicit integration method, but other integration schemes could also be used.

### 5.1 Example scenario

Here, we present the dynamics of an isolated strike-slip fault configuration illustrated in Fig. 2. The fault is just beneath the surface, covering a rectangular area of  $L_x \times L_z$  in the  $x$ - and  $z$ -directions, respectively. We also assume that the fault is adequately oriented in the tectonic stress regime for a slip to occur. For the discretization of the fault area, we use a regular mesh with  $N_x$  elements along the  $x$ -axis and  $N_z$  elements along the  $z$ -axis. Therefore, the total number of elements covering the fault area is  $N = N_x \times N_z$  with each element’s size being  $D_x \times D_z$ , where  $D_x = \frac{N_x}{L_x}$  and  $D_z = \frac{N_z}{L_z}$ .

This system shares the same formulation as Eq. (1) with the internal force vector  $F_{int}$  specified by:

$$F_{int} = K(v_\infty t - d) + H(v_\infty - v), \quad (7)$$

where  $K \in \mathbb{R}^{N \times N}$  is the elasticity matrix,  $H \in \mathbb{R}^{N \times N}$  is the viscosity matrix,  $v_\infty \in \mathbb{R}^N$  is a far-field velocity that continuously strains the system and  $d \in \mathbb{R}^N$  is the displacement of the fault. A lumped mass matrix  $M = \rho L_y D_x D_z I_N$  was used in order to represent the mobilized mass during abrupt slip, where  $I_N$  is the identity matrix of size  $N$  and  $\rho$  is the density. Furthermore, the viscosity matrix  $H = 2\xi M \sqrt{M^{-1}k}$  where  $\xi$  is the damping ratio, and the square root is defined for matrices. Finally, the elasticity matrix  $K = GK_{con}$  where  $G$  is the shear modulus and  $K_{con}$  is the connectivity matrix derived from [34]. For more details, we refer to [35, 36]. Furthermore, the constraint force given by Coulomb friction is typically defined by the closed convex cone

$$C = \{(F_r, q) \in \mathbb{R} \times \mathbb{R}_+ \mid |F_r| \leq q\}, \quad (8)$$

where  $q = \mu(\delta, |v|)A\sigma'_n$  represents a hardening variable determined by the frictional coefficient  $\mu(\delta, |v|)$ , where  $\delta$  is the time-integrated value of  $|v|$  (or slip) and normal force  $A\sigma'_n$  is given by the area and normal effective stress to the fault plane.

In this work, we chose slip weakening law [37]

$$\mu = \mu_d + \Delta\mu e^{-\delta/d_c}, \quad (9)$$

where  $\mu_d$  is the dynamic friction value,  $\Delta\mu$  is the difference between static and dynamic friction, and  $d_c$  is the critical sliding distance. Alternative friction laws could be used, such as in [35], but this would not alter the conclusions of this paper.

The complete set of material parameters for the strike-slip fault is presented in Table 2, where the maximum estimated velocity  $v_{\max}^{\text{est}}$  determined in the same manner as in [33], which was used to normalize the observational average velocity. Additionally, the internal energy at the point of frictional instability was used to normalize the observational average internal energy.

Table 2: (a) Material and geometric parameters for the fault used for simulations unless otherwise specified. (b) Parameters for the friction and predicted earthquake velocity.

(a)						
$L_x = L_y = L_z$ [km]	$G$ [GPa]	$(\sigma'_n)_{\text{avg}}$ [MPa]	$\rho$ [kg/m <sup>3</sup> ]	$\nu$ [-]	$\zeta$ [-]	$v_\infty$ [cm/year]
3	30	22.5	2500	0.25	0.27	0

(b)			
$\Delta\mu$ [-]	$\mu_{\text{res}}$ [-]	$d_c$ [mm]	$v_{\max}^{\text{est}}$ [m/s]
0.1	0.5	100	0.07

### 5.1.1 RL training and heuristic parameters specifics

The TQC network is trained on a fault specified by Table 2 on the basis of discretization with only one element, i.e.,  $D_x = D_z = L_x = L_z$  and we use a continuous action space  $h \in [0.001, \frac{t_{max}}{4}]$  [s]. The bounds were chosen such that  $h_{min}$  would always converge and  $h_{max}$  would result in a single time step for the simulation.

Although a single element is not representative of a finely discretized simulation, it provides two advantages for training the TQC network. First, it provides a relatively fast simulation time during training. Second, it enables exploration of how well the proposed RL-based adaptive policy generalizes to finer discretizations.

Finally, the parameters used for the heuristic time-stepper shown in Table 3 were determined by trial and error for the best performance in all simulated scenarios. Note that despite Bathe’s method having an integration order  $p = 2$  for smooth systems [26], we opted for  $p = 1$  to account for integration reduction observed found in both nonsmooth systems [2] and stiff systems [10]. Additionally, a small initial time step was taken to ensure that the first step converged. Given that the heuristic stepper will reduce the time step until convergence, this choice in the initial time step was found to result in a faster and slightly more accurate integration.

Table 3: Heuristic adaptive time-stepper hyperparameters.

Hyperparameter	Value
Integrator order ( $p$ )	1
Minimum time-step ( $h_{min}$ )	0.001 [s]
Maximum time-step ( $h_{max}$ )	$\frac{t_{max}}{4}$ [s]
Time-step increasing scaling factor ( $h_{up}$ )	2.
Time-step decreasing scaling factor ( $h_{down}$ )	0.6
Initial time step	$0.1 \times \frac{t_{max}}{4}$ [s]

## 5.2 Computation speed

To evaluate the general speed performance, we explore the scenarios for two different fault sizes of 3 [km] by 3 [km] and 5 [km] by 5 [km]. For each fault, we consider mesh discretizations varying from 25, 50, 75, and 100 square elements.



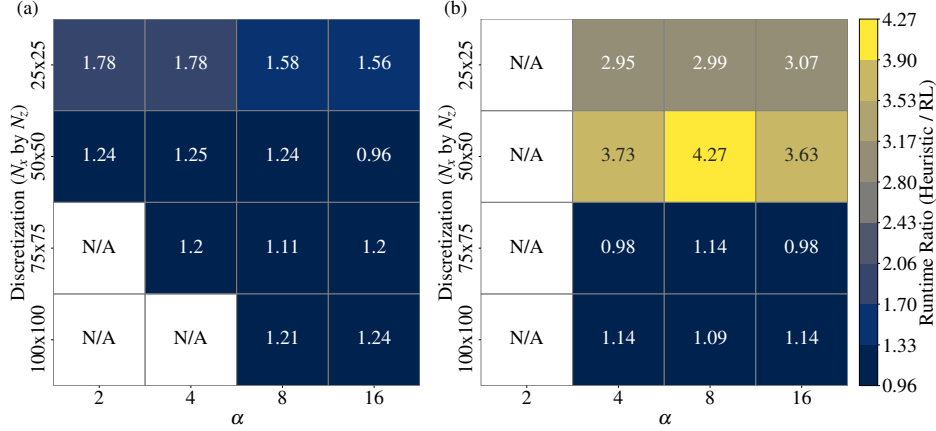


Figure 3: Results demonstrating the ratio of the runtime of the heuristic-based method over the runtime of the RL-based method for (a)  $L_x = L_y = L_z = 3$  [km] fault and (b)  $L_x = L_y = L_z = 5$  [km] fault. The x-axis depicts the speed-accuracy trade-off parameter  $\alpha$  (see Eq. (6)), and the y-axis depicts the fault discretization ( $N_x$  by  $N_z$ ). Note that the white boxes with the “N/A” text indicate that scenarios in the RL-based integrator did not converge.

The computational speed was measured by Python’s time package, and we averaged 10 simulations to reduce variability due to background processes. Additionally, to further minimize variance introduced by background processes, the code was given the highest priority possible on the laptop.

Fig. 3 displays a tile plot for (a) fault configuration of  $L_x = L_y = L_z = 3$  [km] and (b) fault configuration of  $L_x = L_y = L_z = 5$  [km], where the y-axis represents different discretizations, the x-axis shows the values of the speed-accuracy trade-off parameter  $\alpha$ , and the color indicates the ratio of runtimes of the heuristic and RL time-steppers. Note that “N/A” in gray color indicates scenarios where the RL-based policy did not converge. Here, non-convergent indicates that the RL-based policy continuously selected a time step that did not converge, and therefore, the simulation was terminated.

Fig. 3 (a) shows that aside from a single simulation, the RL-based policy is consistently faster than the heuristic-based policy. However, the relative speed advantage tends to reduce slightly as the mesh is refined. Regardless, the average improvement of speed was roughly 1.3 times that of the heuristic for convergent scenarios. Interestingly, the speed advantage does not monotonically decrease with increasing  $\alpha$ , indicating nontrivial dependence on this parameter and potentially slight variances in the training as a result of the stochastic nature of the TQC network.

Fig. 3 (b) shows that the RL-based algorithm also performs well on the 5 [km] by 5 [km] fault, despite never being trained on that configuration. For  $\alpha \geq 4$ , it generally runs faster than the heuristic time-stepper. Although its speed advantage tends to decline as the discretization becomes finer, the RL-based approach remains approximately 2.26 times faster than the heuristic for convergence scenarios.

To better understand why the RL-based simulation is generally faster, we examine the time steps selected by both approaches in the 3 [km] by 3 [km] scenario with a 50 by 50 mesh discretization, which also corresponds to the scenario in Fig. 5. Fig. 4 displays the time steps attempted by each approach over time, with red points representing non-convergent steps and blue points indicating convergent steps. The heuristic approach frequently attempts several time steps  $h$  that do not converge, followed by a reduction until it finds a convergent step. In contrast, Fig. 4 (b) shows that the RL-based approach maintains a more consistent time step, only attempting two steps that did not converge before reducing the time step. Thus, we observe that the RL-based approach learned to maintain nearly constant time steps during slip events followed by a steady increase before plateauing at the sticking phase. This contrasts with the heuristic-based approach, which always tries to maximize the time step. As a result, the heuristic approach experiences more non-convergent steps than the RL approach in this scenario. The apparent state-dependent strategy of the RL-based approach likely explains the improved speed in Fig. 3 (b), as the RL-based policy leverages information of the average state of velocity and internal energy to choose its time steps.

### 5.3 Accuracy

The RL-based method, on average, provides faster simulations than the heuristic-based method, but a critical aspect is if it maintains accuracy. Here, accuracy is taken to be with respect to the constant time stepper when  $h = 0.05$  [s] as there is no closed-form solution to the scenarios explored within this paper.

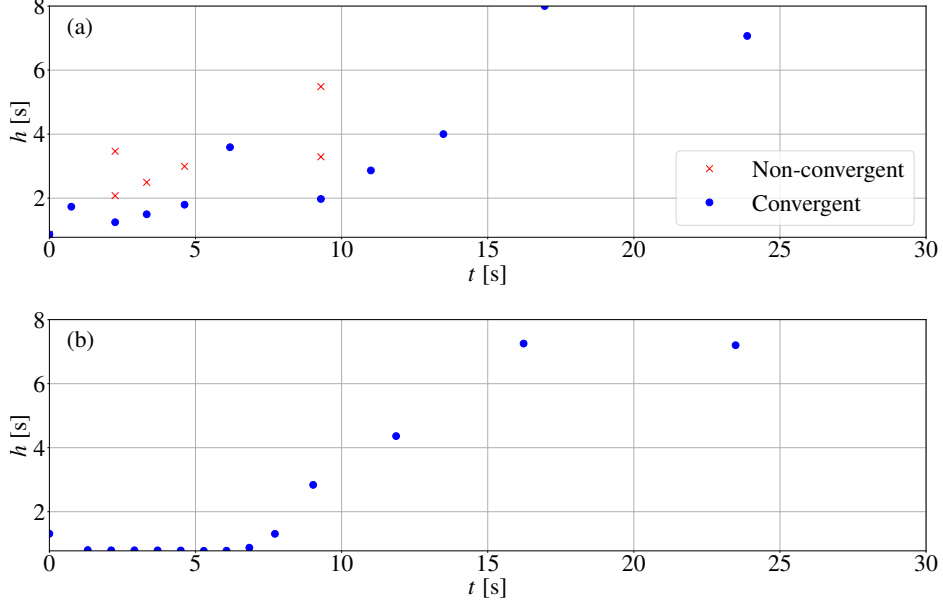


Figure 4: Time step  $h$  choice against time  $t$  for the (a) heuristic time-stepper and (b) the RL-based approach.

To begin, we illustrate the accuracy of both the RL-based and heuristic-based methods for a single scenario. The accuracy of the proposed RL-based time-stepping policy is first explored for a fault with a 50 by 50 element discretization and the speed-accuracy trade-off parameter  $\alpha = 8$ .

Fig. 5 (a) and (b) compare the RL-based method results of the average spatial velocity and average spatial slip overtime against the heuristic method and constant time-stepping methods. By visual inspection, the RL-based method performs similarly to the heuristic method in terms of both the average spatial velocity and the average time integrated slip rate. In Fig. 5 (c) spatial velocity profile is displayed for the RL-based method at  $t = 8.6$  [s] and Fig. 5 (d) shows the relative error,  $(v - v_{true})/v_{true} \times 100$ , where  $v_{true}$  is assumed to be given by the spatial profile of the constant time-stepper for  $h = 0.05$  [s]. The maximum absolute error is roughly 16 % in the whole of the fault and roughly amounts to a deviation of roughly 0.007 [m/s]. This preliminary evaluation suggests that both methods are relatively accurate, though a more comprehensive comparison is necessary to fully gauge accuracy across multiple scenarios.

For a more extensive evaluation, the accuracy is evaluated for the same scenarios displayed in Section 5.3. Fig. 6 displays the relative error of the slip for the RL-based method in the top row via the color bar, and in the bottom row, its performance relative to the heuristic-based method is shown by the color bar. Fig. 6 (a) shows that the RL-based method maintains a good accuracy as the average relative error is approximately 3.26 %. The highest relative error in all convergent scenarios is 10.11 %, which corresponds to a deviation of roughly 24 [mm]. Furthermore, Fig. 6 (b) demonstrates that even for a fault configuration not included in the training set, the RL-based method remains accurate with an average relative error of 3.15 %. Notably, the relative error actually tends to decrease as the mesh discretization is refined.

Fig. 6 (c) and (d) show that relative performance of accuracy varies significantly across scenarios, ranging from one-quarter to nearly four times as accurate as the heuristic-based method. On average, for scenarios in Fig. 6 (c), the RL-based method is 1.31 times more accurate than that of the heuristic-based approach. For the fault configuration of 5 [km] by 5 [km], the RL-based approach is 1.11 times more accurate on average than the heuristic-based approach. These results demonstrate that, for convergent scenarios, the RL-based method not only offers a speed advantage but also tends to be more accurate. Even in scenarios where the RL-based method is less accurate than the heuristic method, it is important to emphasize that it remains reliable, as shown by Fig. 6 (a) and (b).

## 5.4 Proficiency

From the analysis of speed and accuracy, it is evident that the RL-based method generally outperforms the heuristic method in terms of speed and accuracy. To better understand the overall performance, we introduce a measure of proficiency. Here, proficiency is assessed by the multiplication of the run time ratio and the relative error ratio. While

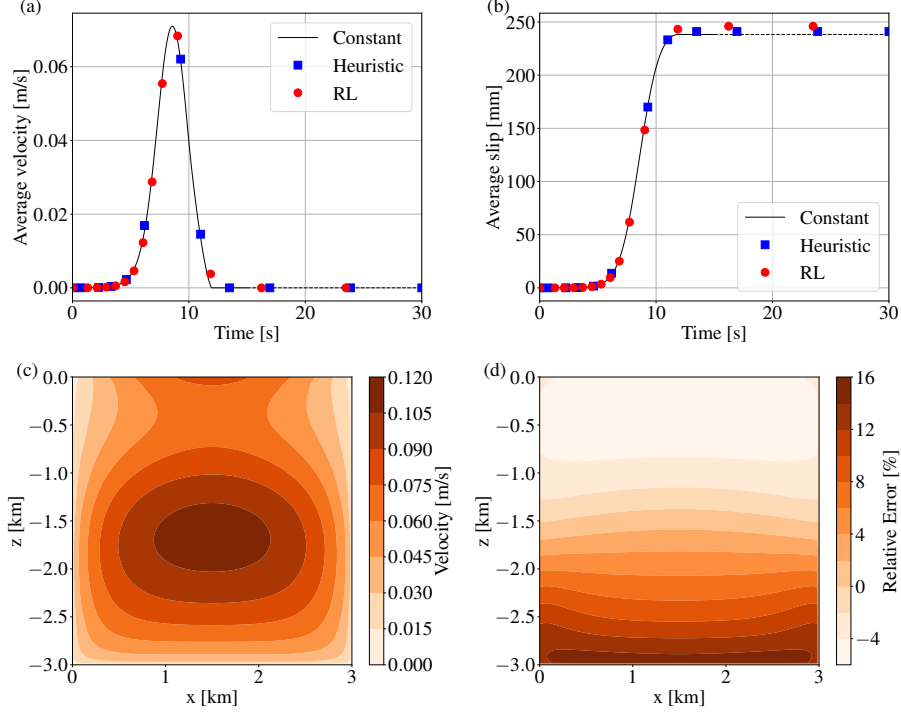


Figure 5: Accuracy of the RL-based adaptive time-stepping approach for a frictional instability not in the RL training set. (a) Average velocity over time for three integration methods: constant time step ( $h = 0.05$  [s]), heuristic, and RL-based. (b) Average slip in time for the three integrators. (c) Velocity spatial distribution snapshot at  $t = 8.6$  [s] using the RL-based integrator. (d) Relative error spatial distribution snapshot between the RL-based and constant time step integration. Note a dashed line shows the asymptotic average values of velocity and slip of the constant time-stepper.

several proficiency measures could be applied, the chosen measure is well-suited to showcasing the balance between error and computational speed, similar to that of the chosen reward function (6).

Fig. 7 (a) displays the proficiency ratio for a fault size 3 [km] by 3 [km]. The proficiency ratio is defined as the heuristic proficiency divided by the RL proficiency, and thus, a value above one indicates that the RL-based method is more proficient. By observation, the RL-based method is more proficient than the heuristic time-stepper in the majority of the simulation scenarios. Notably, the proficiency is lowest for the 50 by 50 discretization scenario but improves at finer discretizations. Thus, the RL-based method achieves a better balance of speed and accuracy than the heuristic-based method. This was achieved despite applying optimizations to the heuristic adaptive time-stepper, such as setting the order of the integrator  $p = 1$  and using a smaller initial time-step that was known a priori to be nearly the largest convergent time step possible for the first increment.

Fig. 7 (b) further shows that for a fault configuration on which the TQC network was not trained, the RL-based method still provides a much more proficient solution than the heuristic-based method. In fact, across these two fault configurations, the RL-based method is 2.12 times more proficient on average. These results show that the RL-based method produces a time-integration approach capable of achieving a proficient integration in a more general and adaptable manner.

## 5.5 Transfer learning

While the previous sections showcased that the RL-based method offers an advantage in speed and accuracy over the heuristic-based method, it also revealed a drawback, i.e., a lack of robustness. Specifically, there were seven scenarios in which the RL-based time stepper did not converge. This is not unexpected since the spatiotemporal frictional instability becomes more complex as the mesh is refined. Although using non-deterministic time steps may reduce the non-convergence, its stochastic behavior produces inconsistent results. However, training the TQC network further on a more finely discretized simulation (transfer learning) can successfully alleviate the convergence problem. The trained TQC network for  $\alpha = 2$  undergoes additional training on a new scenario (transfer learning). The new scenario is for a

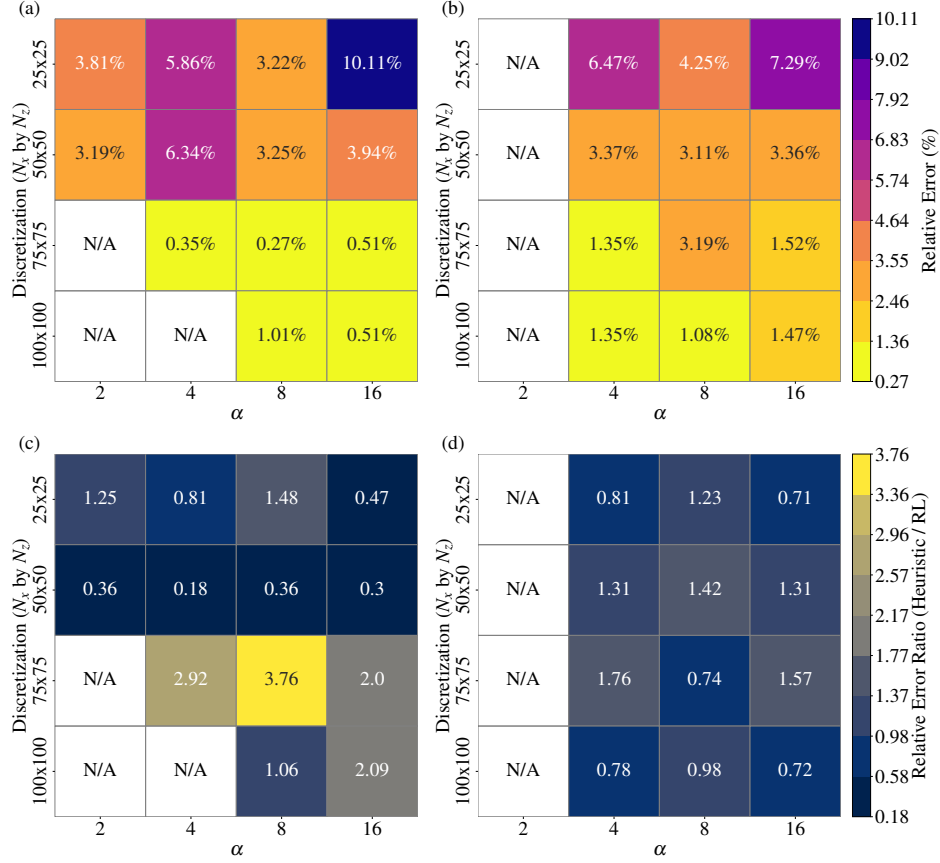


Figure 6: Relative error of the spatial average of the time-integrated slip rate of the RL-based method (top row) for (a)  $L_x = L_y = L_z = 3$  [km] fault and (b)  $L_x = L_y = L_z = 5$  [km] fault and ratio of relative error of the heuristic and the RL-based method for (c)  $L_x = L_y = L_z = 3$  [km] fault and (d)  $L_x = L_y = L_z = 5$  [km]. The x-axis depicts the speed-accuracy trade-off parameter  $\alpha$  (see Eq. (6)), and the y-axis depicts the fault discretization ( $N_x$  by  $N_z$ ). Note that the white boxes with the “N/A” text indicate that scenarios in the RL-based integrator did not converge.

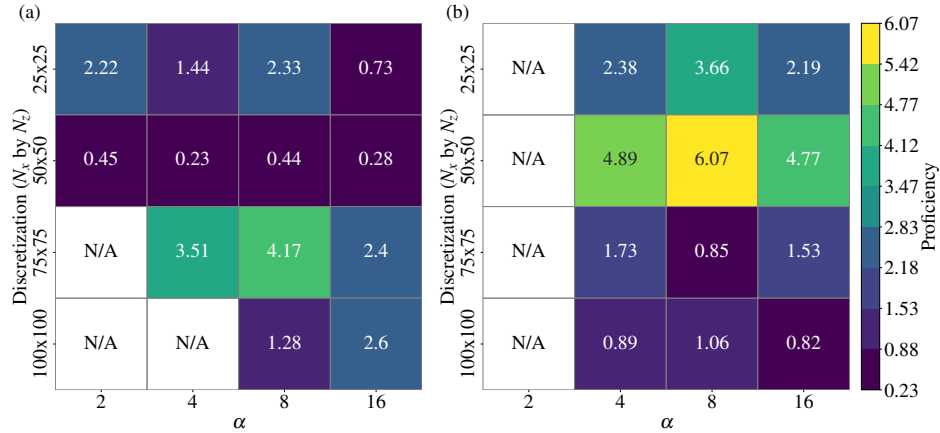


Figure 7: Results demonstrating the ratio of proficiency (color bar), which is taken to be the multiplication of the run time ratio and the relative error ratio for the heuristic method over that of the RL-based method, for (a)  $L_x = L_y = L_z = 3$  [km] fault and (b)  $L_x = L_y = L_z = 5$  [km] fault. The x-axis depicts the speed-accuracy trade-off parameter  $\alpha$  (see Eq. (6)), and the y-axis depicts the fault discretization ( $N_x$  by  $N_z$ ). Note that the white boxes with the “N/A” text indicate that scenarios in the RL-based integrator did not converge.

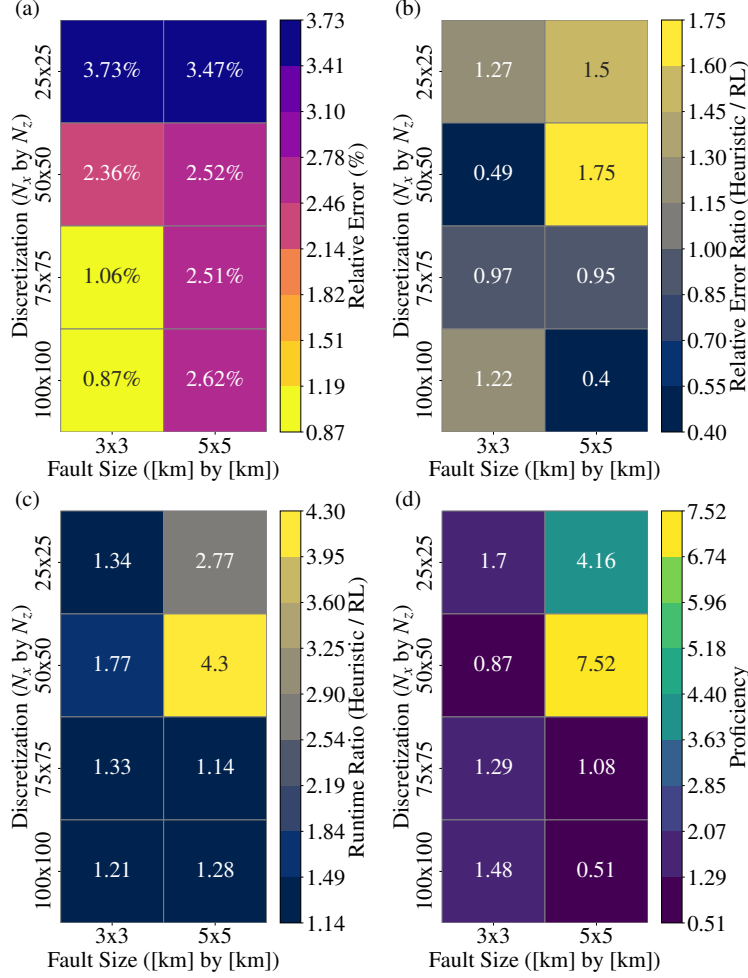


Figure 8: Results demonstrating the transfer learning improvement for the speed-accuracy trade-off parameter  $\alpha = 2$  (see Eq. (6)). The x-axis depicts the fault size ([km] by [km]), and the y-axis depicts the fault discretization ( $N_x$  by  $N_z$ ). (a) Relative error (color bar) of the total slip for the RL-based adaptive time-stepping at the end of the simulation. (b) Ratio of the heuristic relative error to the RL relative error (color bar). (c) Ratio of the heuristic computation time to the RL computation time (color bar). (d) Proficiency measure (color bar), defined as the product of the heuristic relative-error ratio and the heuristic computation-time ratio.

fault with  $L_x = L_y = L_z = 3$  [km] configuration and with a discretization of 30 by 30 elements. By applying further training rather than solely training on a 30 by 30 element discretization, transfer learning provides similar performance but takes considerably less time, as shown in A.

Fig. 8 displays a tile plot of the results from the transfer learning, where the y-axis represents different discretizations, the x-axis shows fault size, and the color indicates (a) the relative error of the final slip, (b) the ratio of the relative errors of the heuristic and RL time-steppers, and (c) the ratio of runtimes of the heuristic and RL time-steppers. Numerical values are displayed on each tile for precision. Most notably, the results demonstrate that after transfer learning, all scenarios for  $\alpha = 2$  now achieve convergence. Moreover, the RL-based method is faster for these scenarios while having a maximum relative error of 3.47%. Furthermore, for the cases that did previously converge, the relative error decreases slightly while maintaining the speed advantage, leading to an overall improvement in proficiency. These results showcase that further training of the TQC enhances robustness while retaining the speed benefits of the RL-based method.

## 6 Conclusions

Our study demonstrates that reinforcement learning (RL), specifically using the Truncated Quantile Critics (TQC) algorithm with a continuous action space, can effectively learn adaptive time-stepping policies for nonsmooth dynamical systems. More specifically, by allowing the RL agent to select time steps within a continuous range in an isolated seismic fault system with set-valued, Coulomb friction, the method generalizes well to different mesh discretizations and fault configurations, even when trained on a single element for a single slip scenario. This results in an efficient training procedure for rapid deployment.

Moreover, the RL-based approach outperforms traditional heuristic adaptive time-stepping methods in terms of computational speed and accuracy. This is particularly evident in complex scenarios like the seismic fault model, where the RL policy adapts to rapid changes in system dynamics more effectively than conventional methods. In particular, our approach achieved a fourfold speed-up, compared to the more conventional heuristic integration scheme. However, the RL-based method experienced convergence issues when some fault discretizations were encountered. The convergence issues were proven to be resolved via transfer learning, which also generally maintains the speed advantage, garnered from the RL-based method.

Notably, the neural network environment requires only information on internal energy and a potential maximum velocity, suggesting that it should generalize well to other mechanical systems. Future works could explore a wider range of frictional systems, contact mechanics, and elastoplasticity. Furthermore, in the context of constitutive modeling of elastoplasticity, the formulations could be expressed as variational inequalities [38, 39] or equivalently a normal inclusion [40], allowing for the application of RL-based adaptive time integration. Finally, investigating the impact of different reward function designs and hyperparameter choices on the learning process could further enhance the performance of RL-based adaptive time-stepping.

### Declaration of competing interest

The authors declare that they have no known competing financial interests or personal relationships that could have appeared to influence the work reported in this paper.

### CRedit authorship contribution statement

**David Riley:** Formal analysis, Investigation, Methodology, Software, Validation, Visualization, Writing – original draft. **Alexandros Stathas:** Methodology, Validation, Supervision, Writing – review & editing. **Diego Gutiérrez-Oribio:** Methodology, Validation, Supervision, Writing – review & editing. **Ioannis Stefanou:** Conceptualization, Methodology, Validation, Supervision, Project administration, Funding acquisition, Writing – review & editing.

### Data availability

Codes accompanying this manuscript will be made publicly available upon acceptance of this manuscript.

### Acknowledgements

David Riley, Diego Gutiérrez-Oribio, and Ioannis Stefanou want to acknowledge the European Research Council’s (ERC) support under the European Union’s Horizon 2020 research and innovation programme (Grant agreement no. 101087771 INJECT). Alexandros Stathas, Diego Gutiérrez-Oribio, and Ioannis Stefanou want to acknowledge the Region Pays de la Loire and Nantes Métropole under the Connect Talent programme (CEEV: Controlling Extreme Events—Blast: Blas LoAds on SStructures).

### References

- [1] Brogliato, B. *Nonsmooth mechanics*. Vol. 3. Springer, 1999.
- [2] Acary, V. and Brogliato, B. *Numerical methods for nonsmooth dynamical systems: applications in mechanics and electronics*. Springer Science & Business Media, 2008.
- [3] Bernardo, M., Budd, C., Champneys, A. R., and Kowalczyk, P. *Piecewise-smooth dynamical systems: theory and applications*. Vol. 163. Springer Science & Business Media, 2008.

- [4] Belykh, I., Kuske, R., Porfiri, M., and Simpson, D. J. “Beyond the Bristol book: Advances and perspectives in non-smooth dynamics and applications”. In: *Chaos: An Interdisciplinary Journal of Nonlinear Science* 33.1 (2023).
- [5] Shtessel, Y., Edwards, C., Fridman, L., and Levant, A. *Sliding Mode Control and Observation*. Intuitive theory of sliding mode control. New York, USA: Birkhauser, 2014.
- [6] Hairer, E., Nørsett, S. P., and Wanner, G. *Solving Ordinary Differential Equations I: Nonstiff Problems*. Vol. 8. Springer Series in Computational Mathematics. Berlin, Heidelberg: Springer, 1993. DOI: <https://doi.org/10.1007/978-3-540-78862-1>.
- [7] Fehlberg, E. *Low-order classical Runge-Kutta formulas with stepsize control and their application to some heat transfer problems*. Vol. 315. National aeronautics and space administration, 1969.
- [8] Press, W. H., Teukolsky, S. A., Vetterling, W. T., and Flannery, B. P. “Numerical Recipes: The Art of Scientific Computing”. In: 3rd. New York, NY, USA: Cambridge University Press, 2007. Chap. 17, pp. 910–928.
- [9] Acary, V. “Toward higher order event-capturing schemes and adaptive time-step strategies for nonsmooth multibody systems”. PhD thesis. INRIA, 2009.
- [10] Söderlind, G. “Automatic control and adaptive time-stepping”. In: *Numerical Algorithms* 31 (2002), pp. 281–310.
- [11] Pfau, R. U. “A priori step size adaptation for the simulation of non-smooth systems”. In: *Communications in numerical methods in engineering* 23.2 (2007), pp. 85–96.
- [12] Ogata, K. *Modern Control Engineering*. 5th. Upper Saddle River, NJ: Pearson, 2020. ISBN: 978-0136156734.
- [13] Gustafsson, K. “Control theoretic techniques for stepsize selection in explicit Runge-Kutta methods”. In: *ACM Transactions on Mathematical Software (TOMS)* 17.4 (1991), pp. 533–554.
- [14] Chen, R. T., Rubanova, Y., Bettencourt, J., and Duvenaud, D. K. “Neural ordinary differential equations”. In: *Advances in neural information processing systems* 31 (2018).
- [15] Liu, Y., Kutz, J. N., and Brunton, S. L. “Hierarchical deep learning of multiscale differential equation time-steppers”. In: *Philosophical Transactions of the Royal Society A* 380.2229 (2022), p. 20210200.
- [16] Dellnitz, M., Hüllermeier, E., Lücke, M., Ober-Blöbaum, S., Offen, C., Peitz, S., and Pfannschmidt, K. “Efficient time-stepping for numerical integration using reinforcement learning”. In: *SIAM Journal on Scientific Computing* 45.2 (2023), A579–A595. DOI: 10.1137/21M1412682.
- [17] Han, C., Zhang, P., Bluestein, D., Cong, G., and Deng, Y. “Artificial intelligence for accelerating time integrations in multiscale modeling”. In: *Journal of computational physics* 427 (2021), p. 110053.
- [18] Zhu, Y., Han, C., Zhang, P., Cong, G., Kozloski, J. R., Yang, C.-C., Zhang, L., and Deng, Y. “AI-aided multiscale modeling of physiologically-significant blood clots”. In: *Computer Physics Communications* 287 (2023), p. 108718.
- [19] Dong, Y., Niu, D., Jin, Z., Zhang, C., Li, Q., and Sun, C. “Adaptive stepping pta for dc analysis based on reinforcement learning”. In: *IEEE Transactions on Circuits and Systems II: Express Briefs* 70.1 (2022), pp. 266–270.
- [20] Xu, L., Niu, D., Yang, Y., Wang, A., Jin, Z., Dong, Y., and Zhang, C. “Adaptive Transient Stepping Policy on Reinforcement Learning”. In: *2023 International Symposium of Electronics Design Automation (ISED)*. IEEE, 2023, pp. 46–51.
- [21] Kuznetsov, A., Shvechikov, P., Grishin, A., and Vetrov, D. “Controlling overestimation bias with truncated mixture of continuous distributional quantile critics”. In: *International Conference on Machine Learning*. PMLR, 2020, pp. 5556–5566.
- [22] Crisfield, M. A. *Non-linear Finite Element Analysis of Solids and Structures: Volume 2—Advanced Topics*. Vol. 2. Chichester, England: John Wiley & Sons Ltd, 1997, pp. 411–444. ISBN: 0-471-95649-X.
- [23] Bauchau, O. A. and Laulusa, A. “Review of Contemporary Approaches for Constraint Enforcement in Multibody Systems”. In: *Journal of Computational and Nonlinear Dynamics* 3.1 (Nov. 2007), p. 011005. ISSN: 1555-1415. DOI: 10.1115/1.2803258.
- [24] Laulusa, A. and Bauchau, O. A. “Review of Classical Approaches for Constraint Enforcement in Multibody Systems”. In: *Journal of Computational and Nonlinear Dynamics* 3.1 (Nov. 2007), p. 011004. ISSN: 1555-1415. DOI: 10.1115/1.2803257.
- [25] Acary, V., Brémond, M., and Huber, O. “On solving contact problems with Coulomb friction: formulations and numerical comparisons”. In: *Advanced Topics in Nonsmooth Dynamics: Transactions of the European Network for Nonsmooth Dynamics* (2018), pp. 375–457. DOI: 10.1007/978-3-319-75972-2\_10.
- [26] Bathe, K.-J. and Noh, G. “Insight into an implicit time integration scheme for structural dynamics”. In: *Computers & Structures* 98 (2012), pp. 1–6. DOI: <https://doi.org/10.1016/j.compstruc.2012.01.009>.

- [27] Zhang, R., Yu, Y., Wang, Q., and Wang, Q. “An improved implicit method for mechanical systems with set-valued friction”. In: *Multibody System Dynamics* 48 (2020), pp. 211–238. DOI: <https://doi.org/10.1007/s11044-019-09713-0>.
- [28] Sutton, R. S. “Reinforcement learning: An introduction”. In: *A Bradford Book* (2018).
- [29] Stathas, A., Gutiérrez-Oribio, D., and Stefanou, I. “Introduction to Reinforcement Learning with Applications in Geomechanics”. In: *Machine Learning in Geomechanics 2*. John Wiley & Sons, Ltd, 2024. Chap. 4, pp. 101–184. ISBN: 9781394325665. DOI: <https://doi.org/10.1002/9781394325665.ch4>.
- [30] Gutiérrez-Oribio, D., Stathas, A., and Stefanou, I. “AI-Driven Approach for Sustainable Extraction of Earth’s Subsurface Renewable Energy While Minimizing Seismic Activity”. In: *International Journal for Numerical and Analytical Methods in Geomechanics* (2024). DOI: <https://doi.org/10.1002/nag.3923>.
- [31] Raffin, A., Hill, A., Gleave, A., Kanervisto, A., Ernestus, M., and Dormann, N. “Stable-baselines3: Reliable reinforcement learning implementations”. In: *Journal of Machine Learning Research* 22.268 (2021), pp. 1–8.
- [32] Fujimoto, S., Hoof, H., and Meger, D. “Addressing function approximation error in actor-critic methods”. In: *International conference on machine learning*. PMLR, 2018, pp. 1587–1596.
- [33] Tzortzopoulos, G. “Controlling earthQuakes (CoQuake) in the laboratory using pertinent fault stimulating techniques”. PhD thesis. École centrale de Nantes, 2021.
- [34] Rice, J. R. “Spatio-temporal complexity of slip on a fault”. In: *Journal of Geophysical Research: Solid Earth* 98.B6 (1993), pp. 9885–9907. DOI: <https://doi.org/10.1029/93JB00191>.
- [35] Stefanou, I. and Tzortzopoulos, G. “Preventing instabilities and inducing controlled, slow-slip in frictionally unstable systems”. In: *Journal of Geophysical Research: Solid Earth* 127.7 (2022), e2021JB023410. DOI: <https://doi.org/10.1029/2021JB023410>.
- [36] Gutierrez-Oribio, D., Stefanou, I., and Plestan, F. “Passivity-based control of underactuated mechanical systems with Coulomb friction: Application to earthquake prevention”. In: *Automatica* 165 (2024), p. 111661. DOI: <https://doi.org/10.1016/j.automatica.2024.111661>.
- [37] Kanamori, H. and Brodsky, E. E. “The physics of earthquakes”. In: *Reports on progress in physics* 67.8 (2004), p. 1429.
- [38] Krabbenhøft, K., Lyamin, A., and Sloan, S. “Formulation and solution of some plasticity problems as conic programs”. In: *International Journal of Solids and Structures* 44.5 (2007), pp. 1533–1549.
- [39] Krabbenhoft, K., Lyamin, A., Sloan, S., and Wriggers, P. “An interior-point algorithm for elastoplasticity”. In: *International Journal for Numerical Methods in Engineering* 69.3 (2007), pp. 592–626.
- [40] Guillet, L., Acary, V., Bourrier, F., and Goury, O. “Semi-smooth Newton method for nonassociative plasticity using the bi-potential approach”. In: *16ème Colloque National en Calcul de Structures*. 2024.

## Appendix A. Alternative training scenario

An alternative logic to the training done within Section 5.5 is to train an untrained TQC network directly on the 30 by 30 discretization scenario to provide the robustness that the simple training in Section 5.1.1 did not produce. To investigate this scenario, a TQC network was trained on the scenario of a 30 by 30 element discretization for the same parameters displayed in Table 2 and a speed-accuracy trade-off coefficient  $\alpha = 2$  for a total of 40,000 steps. Note that this network was trained for 40,000, which is the total number of training steps taken in the transfer learning scenario.

Fig. A.1 displays a tile plot of the results from the new training scenario, where the y-axis represents different discretizations, the x-axis shows fault size, and the color indicates (a) the relative error of the final slip, (b) the ratio of the relative errors of the heuristic and RL time-steppers, and (c) the ratio of runtimes of the heuristic and RL time-steppers. Numerical values are displayed on each tile for precision. The first characteristic evident from this plot is that all scenarios converge. Despite the robustness, both the maximum and average relative error are higher for this training scenario than that of the transfer learning scenario, which leads to lower relative error ratios. However, the average runtime ratio is 1.29 times, slightly larger than the average runtime ratio of 1.26 times found in the transfer learning scenario. Finally, the average proficiency is slightly lower than that of the transfer learning case. Fig. A.1 provides evidence that this alternative training scenario is a viable method but less efficient because it requires roughly twice the training time compared to the transfer learning case while providing nearly identical performance. It should be stated that a TQC network trained for only 20,000 steps on the 30 by 30 element discretization was found to converge in all scenarios but performed considerably poorer and, thus, is not explored here.



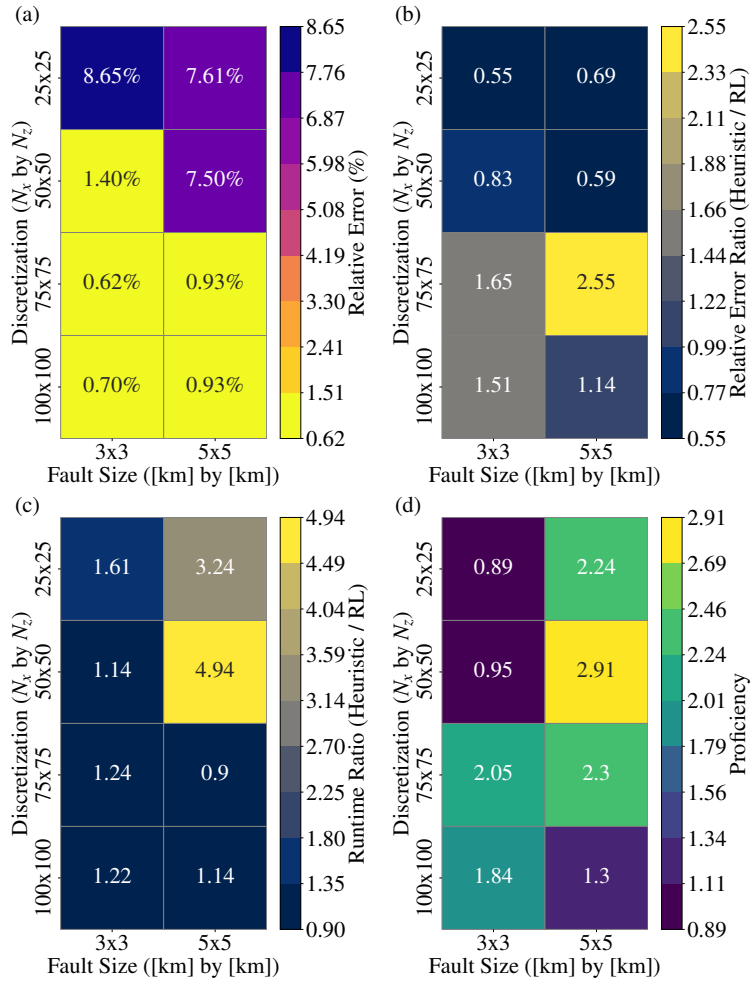


Figure A.1: Results showing the alternative training scenario. The x-axis depicts the fault size ([km] by [km]), and the y-axis depicts the fault discretization ( $N_x$  by  $N_z$ ). (a) Relative error (color bar) of the total slip for the RL-based adaptive time-stepping at the end of the simulation. (b) Ratio of the heuristic relative error to the RL relative error (color bar). (c) Ratio of the heuristic computation time to the RL computation time (color bar). (d) Proficiency measure (color bar), defined as the product of the heuristic relative-error ratio and the heuristic computation-time ratio.